Investigation of X-ray Fluorescence Computed Tomography (XFCT) and K-Edge Imaging

Magdalena Bazalova*, Yu Kuang, Guillem Pratx, and Lei Xing

***Abstract*—This work provides a comprehensive Monte Carlo study of X-ray fluorescence computed tomography (XFCT) and K-edge imaging system, including the system design, the influence of various imaging components, the sensitivity and resolution under various conditions. We modified the widely used EGSnrc/DOSXYZnrc code to simulate XFCT images of two acrylic phantoms loaded with various concentrations of gold nanoparticles and Cisplatin for a number of XFCT geometries. In particular, reconstructed signal as a function of the width of the detector ring, its angular coverage and energy resolution were studied. We found that XFCT imaging sensitivity of the modeled systems consisting of a conventional X-ray tube and a full 2-cm-wide energy-resolving detector ring was 0.061% and 0.042% for gold nanoparticles and Cisplatin, respectively, for a dose of ~ 10 cGy. Contrast-to-noise ratio (CNR) of XFCT images of the simulated acrylic phantoms was higher than that of transmission K-edge images for contrast concentrations below 0.4%.**

***Index Terms*—Computed tomography, medical diagnostic imaging, molecular imaging.**

I. Introduction

X-RAY computed tomography (CT) imaging plays a pivotal role in the diagnosis, staging, treatment planning, and therapeutic assessment of various diseases. It is also indispensable in preclinical small animal imaging research. The modality, however, falls short in providing molecular features. How to add molecular imaging information on top of anatomical CT images represents a significant unmet need in clinical practice and *in vivo* animal imaging studies. A technique using X-ray excitable nanophosphors has been suggested for simultaneous imaging of anatomy and molecular features [1]–[3]. While the approach shows extremely high sensitivity and spatial resolution, limited penetration depth of optical signal may render the X-ray luminescence CT (XLCT) to preclinical use and certain niche clinical applications.

An alternative approach is X-ray fluorescence computed tomography (XFCT), which aims to generate molecular contrast by detecting the characteristic K_α X-rays from the interaction between X-ray and the probe(s) containing high atomic number element, such as the gold nanoparticles [4], [5] and iodine [6]. The 3-D distribution of the high-Z contrast agent within the object is tomographically reconstructed based on the measured fluorescence sinogram data obtained using photon-counting detectors [7]. Up to this point, this modality has not been fully investigated and there is a general need for a comprehensive understanding of the X-ray fluorescence imaging system, its dependence on the type of contrast agent, and its achievable sensitivity and spatial resolution.

In this work, we carry out a detailed Monte Carlo study of the fluorescence imaging system using different phantoms containing either gold nanoparticles [8] or Cisplatin [9] and shed useful insight into the optimal design of XFCT. Historically, CT has been used for imaging of high-Z materials in two other ways, using dual-energy CT [10], [11], in which atomic numbers and mass densities of each voxel are calculated based on CT scans taken at two energies, and K-edge imaging [12], in which photons with energies above the K_{edge} of high-Z agents are used for image reconstruction. Dual-energy CT imaging is a promising technique, however, it has not been used preclinically due to high image noise and motion artifacts. For comparison purposes K-edge imaging is also simulated along with the XFCT studies.

II. Materials and Methods

A. Simulation Geometry

The simulation geometry of XFCT and transmission CT K-edge imaging is shown in Fig. 1. Phantoms containing the contrast media were scanned with an X-ray pencil beam in the first generation CT geometry. The rectangular 0.5 mm 110 kV beam traveled along 5.5 cm using 110 dwell positions before the beam was rotated by 1° over a full 360° rotation. An energy resolving detector ring with a diameter of 10 cm was simulated. Various angles covered by the detector ring and various widths of the ring were simulated. The energy resolution of the detector ring was also modified in order to evaluate the effect of detector energy resolution on image quality. Images acquired with various imaging doses were simulated.

B. Phantoms

Three cylindrical phantoms, a low-resolution and two high-resolution phantoms, with two contrast media, gold nanoparticles and Cisplatin containing platinum, were simulated. All phantoms were made of acrylic and were 5 cm in diameter and 3 cm in length. The low-resolution phantom [Fig. 2(a)] contained four cylindrical vials with 1 cm in diameter and contrast media with concentrations of 0.5%, 1.0%, 1.5%, and 2.0% (or 5–20 mg of Au or Pt per 1 g of water). The high-resolution phantoms contained sixty cylindrical vials with 0.5, 0.4, 0.3,

Manuscript received April 02, 2012; revised May 05, 2012; accepted May 06, 2012. Date of publication June 05, 2012; date of current version July 27, 2012. This work was supported in part by, from NCI (1R01 CA133474 and 1R21 408 CA153587) and NSF (0854492). *Asterisk indicates corresponding author.*

*M. Bazalova is with the Radiation Oncology Department, Stanford University, Stanford, CA 94305 USA (e-mail: bazalova@stanford.edu).

Y. Kuang, G. Pratx, and L. Xing are with the Radiation Oncology Department, Stanford University, Stanford, CA 94305 USA (e-mail: yukuang@stanford.edu; pratx@stanford.edu; lei@stanford.edu).

Digital Object Identifier 10.1109/TMI.2012.2201165

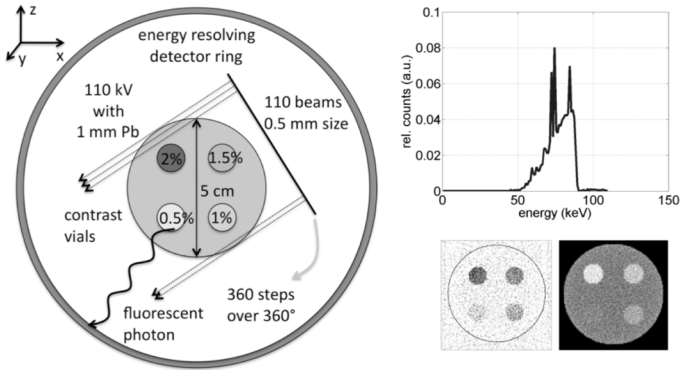

Fig. 1. Simulation setup of X-ray fluorescence and transmission CT imaging. The X-ray source was a 110 kV photon beam (spectrum shown on the right). Examples XFCT and transmission CT images are also presented.

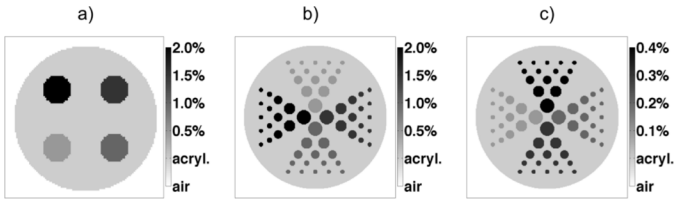

Fig. 2. Schematic drawings of the simulated phantoms. Low-resolution phantom (a) is a 5-cm-diameter acrylic cylinder containing four 1-cm-diameter cylindrical vials with contrast media with concentrations of 0.5%, 1.0%, 1.5%, and 2.0%. Phantom (b) is a high-resolution high-concentration phantom containing vials with diameters of 0.5, 0.4, 0.3, 0.2, 0.15 cm and contrast media with concentrations from 0.5% to 2.0%. Phantom (c) is a high-resolution low-concentration phantom with concentrations ranging from to 0.1%–0.4%.

0.2, and 0.15 cm in diameter and with contrast media concentrations of 0.5%, 1.0%, 1.5%, and 2.0% in the high-concentration phantom [Fig. 2(b)] and with contrast media concentrations of 0.1%, 0.2%, 0.3%, and 0.4% in the low-concentration phantom [Fig. 2(c)].

C. Monte Carlo Simulations

The EGSnrc [13]/BEAMnrc [14] and DOSXYZnrc [15] MC codes were used for all simulations. First, the spectrum of the 110 kV photon beam was simulated in the BEAMnrc code. The entire XFCT imaging geometry was then simulated in the DOSXYZnrc code that we modified for the simulation of CT geometry. Relevant low energy electron and photon physics, such as electron impact ionization, bound Compton scattering, Rayleigh scattering, and atomic relaxations, were included in the simulations that were run on a 2×3 GHz Quad-Core Intel Xeon computer. The most time intensive DOSXYZnrc simulation took approximately seven days using 8 CPUs.

1) Photon Beam Simulations: A small rectangular 0.5×1 mm 110 kV photon beam was used in all simulations. Whereas the 0.5 mm dimension was chosen to achieve high image resolution, the 1 mm dimension parallel to the rotational axis of the cylindrical phantom was chosen for more efficient MC simulations. The 110 kV beam spectrum was simulated in the BEAMnrc code. A 0.1-mm-diameter circular electron beam with 110 keV was incident on a 17-μm-thick tungsten transmission target converting the electron beam into Bremsstrahlung and characteristic X-rays. The beam was then filtered with a 680-μm-thick lead foil to enhance the relative number of photons with energies above the K_{edge} of Au (80.7 keV) and Pt (78.4 keV) using the K_{edge} of Pb at 88.0 keV [5]. The photon beam was then collimated by a 5-cm-thick lead block with 0.5×1 mm opening to approximate a pencil beam used in the next simulation step, as described in the previous paragraph. The energy spectrum of the photons in the phase-space scored below the collimator was used in all simulations. Note that no beam penumbra was included in XFCT simulations, however, due to the large thickness of the collimator the beam penumbra was negligible.

2) XFCT and Transmission CT Geometry Simulations: XFCT geometry was simulated in a version of the DOSXYZnrc code that was modified for simulations of CT geometry. The parallel rectangular beam from multiple directions was chosen as the source to simulate parallel-beam XFCT geometry. The beam was 5.5 cm wide in the xz-plane and 0.1 cm wide in the y-direction and rotated in 1°-steps over 360°. The dosxyznrc.mortran code was modified such as each particle's initial x-coordinate and angle of incidence were recorded. The ausgab routine [15] was modified to calculate the position of each particle leaving the geometry. If the particle interacted with the detector ring, the energy of the particle was stored in the respective position in the sinogram determined based on the particle's incident coordinate along the line of the source and incidence angle. For each event, the incident x and z coordinates of the excitation X-ray photon were recorded. Based on the direction of the photon, the radial position along the source for sinogram sorting was calculated. The tube angle was determined by the original direction of the photon. The history of the photon was tracked and all photons generated by the excitation X-ray photon leaving the geometry were checked whether they interacted with any part of the detector ring. If they did, the count in the energy bin of the energy of the photon leaving the geometry was increased by one at the radial position and tube angle of the incident excitation X-ray photon.

The energy spectrum for each sinogram point was binned in 1 keV bins. Whereas XFCT sinograms did not include photons from the detectors directly opposite of the pencil beam, transmission CT sinograms only consisted of these photons. Both fluorescence and scatter photons were stored in XFCT sinograms. Apart from the default .3ddose dose distribution file, .sinogram files containing the number of photons in each energy bin for each X-ray beam position and angle were also generated as a result of all MC simulation.

3) Detector Ring: The detector ring was first considered as a 2 cm wide full detector ring with an ideal energy response. More realistic cases were studied by altering the detector ring width, angular coverage, and energy response. The effect of the detector ring properties was studied with the low-resolution phantom loaded with platinum and imaged with a dose of 2 mGy.

Additional detector widths of 1 cm, 5 mm, and 3 mm were simulated. The CdTe detector is commercially available with 3×3 mm and 5×5 mm crystals. The intersection of each particle leaving the geometry with the detector ring cylinder was calculated. The y-coordinate of the intersection determined whether the detector ring registered the photon.

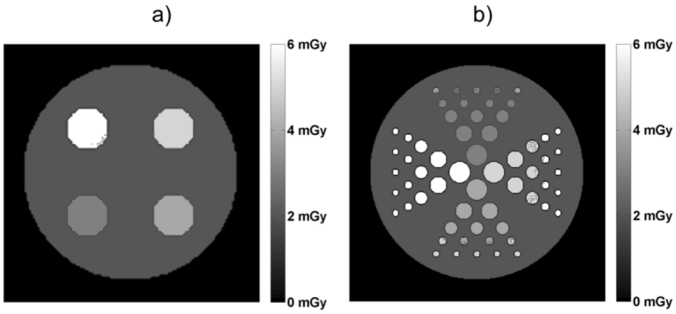

Fig. 3. Imaging dose for the (a) low-resolution and (b) high-resolution phantom loaded with gold nanoparticles. The dose to the center of the phantoms is 2 mGy.

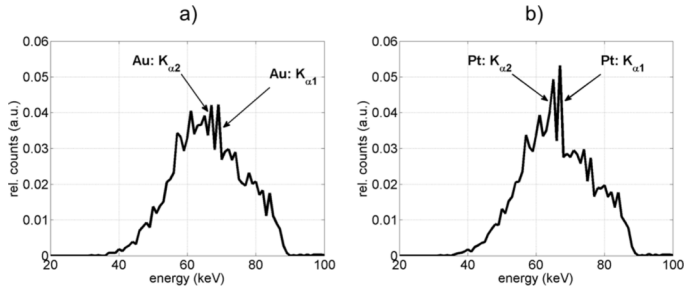

Fig. 4. Energy spectrum for a single sinogram point of the low-resolution phantom loaded with gold (a) and platinum (b) imaged with 0.1 mGy.

The detector angular coverage of 360° ensures the highest efficiency in detecting X-ray fluorescence photons. In order to reduce the detector cost, images reconstructed from detector angular coverage of 240°, 180°, and 90° were studied, reducing the number of detectors by 33%, 50%, and 75%, respectively. The full detector ring was divided into 36 10°-detector blocks and every two out of three detector blocks, every other detector block and every fourth detector block was enabled for X-ray detection using the 240°, 180°, and 90°-detector coverage, respectively. Separate .sinogram files for each detector width and angular coverage were stored.

The detector energy response was studied using post-processing of existing sinograms. The energy spectrum of each sinogram point was blurred with a Gaussian distribution with a standard deviation calculated based on relative energy resolution values of 1.0%, 1.5%, 2.0%, 2.5%, and 3.0%. It has been reported that the energy resolution of the CdTe detector is 1.1% for $^{57}\mathrm{Co}$ (122 keV) [16].

4) Phantom Simulations: The cylindrical phantoms were represented in voxelized geometries as required by the DOSXYZnrc code. The voxel sizes were 500 and 200 $\mu\mathrm{m}$ for the low-resolution and high-resolution phantoms, respectively. The gold nanoparticle media were considered to be simply mixtures of water and gold. Cisplatin solutions were modeled as solutions of water and $\mathrm{H_6Cl_2N_2Pt}$, which is the chemical composition of the drug. The mass densities of the contrast agents were chosen to be 1.001, 1.002, 1.004, 1.004, 1.005, 1.01, 1.015, and 1.02 $\mathrm{g/cm^3}$ for the 0.1%, 0.2%, 0.3%, 0.4%, 0.5%, 1.0%, 1.5%, and 2.0%, concentrations, respectively, for both gold and platinum. Even though the chosen mass densities are somewhat arbitrary, the mass density does not change with such low contrast concentrations, which will not alter the results of the simulations, as the composition is the more important parameter for interactions at kilovoltage photon energies.

The imaging dose to the phantoms was quantified and the dose to the center of the phantom was considered as the imaging dose to the phantom. The dose distributions in both phantoms loaded with gold nanoparticles are shown in Fig. 3. The imaging dose in the center of the phantom is approximately 30% and 25% of the maximum imaging dose for the low and high-resolution phantoms, respectively. The maximum dose deposition occurs in the vials with the highest contrast concentration due to the contribution of the photoelectric effect and the short ranges ($\sim 100\ \mu\mathrm{m}$) of the photoelectrons. Due to the small size of the phantom, the dose difference between the periphery of the phantom and the center of the phantom is within 5%. In order to image the low- and high-resolution phantoms with a dose of 2 mGy, 1.02×10^{10} and 1.08×10^{10} incident photons were simulated, respectively.

D. Image Reconstruction

Parallel beam sinograms containing energy spectra for each sinogram data point were stored as a result of MC simulations and processed to reconstruct XFCT and transmission CT images. MATLAB (The Mathworks, Natick, MA) was used for data processing and image reconstruction. The reconstructed signal was evaluated as the mean value of regions of interest (ROIs) just covering each contrast vial. Contrast-to-noise ratio (CNR) was also evaluated by calculating the ratio of the difference between the mean values of the signal of each ROI and acrylic and the standard deviation of the background signal.

1) XFCT Image Reconstruction: XFCT images were reconstructed using both $K\alpha_1$ and $K\alpha_2$ peaks at 68.8 keV and 67.0 keV for gold and 66.8 keV and 65.1 keV for platinum, respectively. Sample energy spectra from a single sinogram data point (radial position of 1 cm and tube angle of 100°, see Fig. 5) for both gold and platinum are presented in Fig. 4(a) and (b), respectively. The sinogram for XFCT image reconstruction was calculated as the sum of the net $K\alpha$ counts for both fluorescence energies. The fluorescence X-rays are superimposed on Compton scattered photons and the net number of fluorescence X-rays has to be extracted. In general, the Compton scatter contribution can be estimated by interpolation using a number of neighboring energy bins. In our simulations, the number of Compton scatter photons was calculated using a simple linear interpolation based on the number of counts of a single neighboring energy bin on each side. This interpolation works well in the simulated sinogram data due to the 1 keV resolution considering an idealized detector with perfect energy response. The net number of $K\alpha$ counts was then calculated as the total number of counts at the $K\alpha$ energy minus the approximated number of Compton scattered photons.

XFCT images were reconstructed using simple filtered backprojection with the Shepp-Logan filter. The reconstructed signal was normalized using a separately simulated image of a vial containing 2% contrast concentration. XFCT images were reconstructed for both phantoms loaded with both contrast media imaged with various doses using the default 2-cm-wide detector

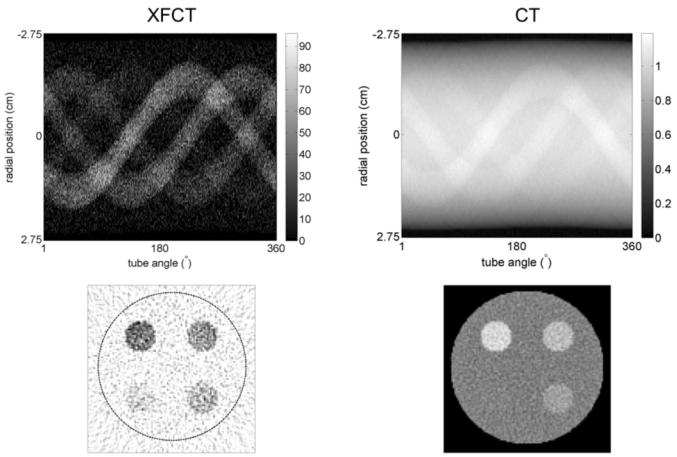

Fig. 5. inograms (top) and reconstructed CT images (bottom) for XFCT (left) and transmission CT (right) of the low-resolution phantom loaded with gold for a 0.1 mGy imaging dose.

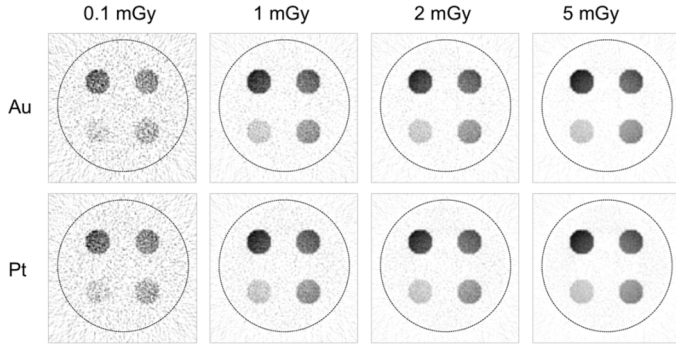

Fig. 6. XFCT images of the low-resolution phantom loaded with gold (top) and platinum (bottom) as a function of imaging dose. Values from 0 to the maximum reconstructed value are displayed in each XFCT image.

ring with a full 360°-coverage and ideal energy resolution. The properties of the detector ring were studied using XFCT images of the low-resolution phantom loaded with platinum and imaged with a 2 mGy dose.

2) Transmission CT Image Reconstruction: Transmission CT images were reconstructed for the high-resolution phantom loaded with both contrast agents imaged with a 2 mGy dose using only transmission data. Sinograms for transmission CT reconstruction were generated in two ways. First, similar to conventional CT scanners, the number of counts of each sinogram point was integrated over the entire energy spectrum. Second, K-edge imaging was performed by subtracting CT images reconstructed using photons below the K_{edge} of the contrast medium ($\mathrm{CT} < K_{\mathrm{edge}}$ images) from conventional CT images reconstructed using the entire energy spectrum. This was done to approximate previous iodine CT K-edge imaging work, in which CT data were acquired at energies below and above the K-edge of iodine and CT images were reconstructed using the difference of the two datasets [17]. For gold and platinum, the K_{edge} energy was considered to be the energy bins 81 and 79, respectively.

The number of counts were converted into projections p using $p = -\ln(I/I_0)$, where I is the number of counts and I_0 is the maximum number of counts found in the sinogram, corresponding to an air-scan. Similar to XFCT, CT images were reconstructed using filtered back-projection of the projection data. The reconstructed data, or the linear attenuation coefficients, were converted into CT numbers using CT number $= 1000 \times (\mu/\mu_w - 1)$, where μ is the linear attenuation coefficient of a voxel and μ_w is the linear attenuation coefficient of water.

III. Results

A. Image Reconstruction

An XFCT sinogram showing the net number of $K\alpha$ counts of the low-resolution phantom loaded with gold and imaged with 0.1 mGy is presented in the left column of Fig. 5. The XFCT image reconstructed from the sinogram data of the gold low-resolution phantom is also shown in Fig. 5. An example of a conventional CT sinogram including photon counts of all energies and the corresponding CT image is shown in the right column of Fig. 5.

B. XFCT Imaging

1) Gold and Platinum: XFCT images of the low-resolution phantom loaded with gold and platinum for various imaging doses are shown in Fig. 6. The image quality for both contrast agents is comparable and the reduction of noise with increasing imaging dose is evident. Nonuniformity of the signal within each vial is also apparent. The vial with 0.5% concentration is just visible in the 0.1 mGy images, however, its contrast is much higher in the images acquired with at least 1 mGy imaging dose.

The reconstructed concentration calculated from the mean value of each vial as a function of true contrast concentration and imaging dose for both gold and platinum is presented in Fig. 7(a) and (b). Gold and platinum concentrations are reconstructed accurately within 1.5% and 2.9% for the 5 mGy XFCT images. The CNR graphs as a function of imaging dose and contrast concentration are shown in Fig. 7(c) and (d). In agreement with the reconstructed signal results presented in Fig. 7(a) and (b), CNR in gold XFCT imagines is lower than in platinum images. The data are fitted with a straight line and the CNR of 4, the detectability limit given by Rose criterion [18], is marked. According to the Rose criterion and based on the simulated setup, 0.20% and 0.19% is the lowest gold and platinum concentration that can be detected in XFCT images acquired with a 5 mGy imaging dose.

2) Detector Ring: The results of the detector ring study are presented in Fig. 8. All data were calculated for the low-resolution phantom loaded with platinum and imaged with a 2 mGy dose. The dependence of CNR on the detector width is shown in Fig. 8(a). A linear relationship between the reconstructed signal and detector width is observed. CNR as a function of detector angular coverage is presented in Fig. 8(b). A linear relationship is observed similar to the detector width study, as expected. The detector energy resolution plot, presented in Fig. 8(c), demonstrates that energy resolution of up to 1.5% does not significantly

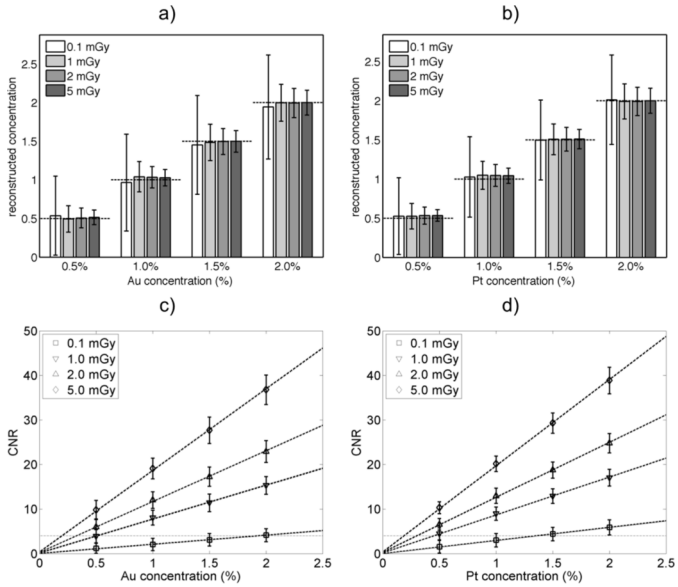

Fig. 7. Reconstructed concentration (a, b) and CNR (c, d) as a function of contrast concentration and imaging dose for gold (a, c) and platinum (b, d) based on simulations of the low-resolution phantom.

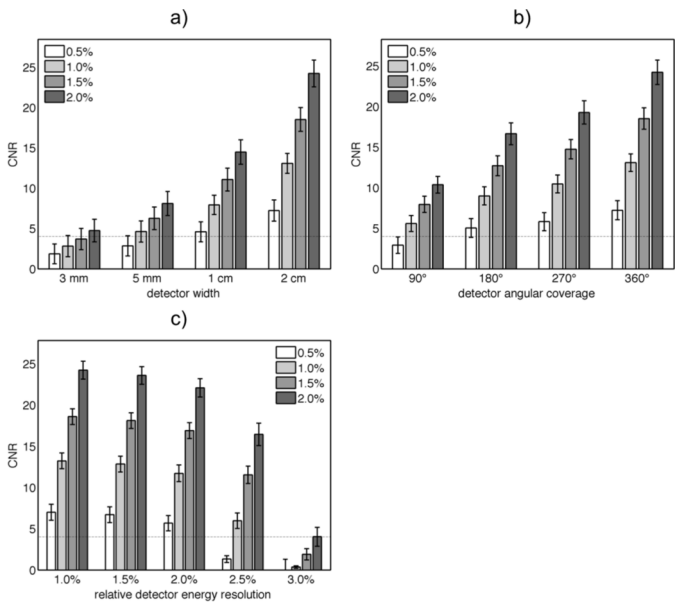

Fig. 8. CNR for four concentrations of platinum as a function of detector width (a), detector angular coverage (b), and detector energy resolution (c) based on the low-resolution phantom imaged with a 2 mGy dose.

affect the quality of XFCT images using the suggested data acquisition setup with 1 keV energy bins. However, the 2.0% concentration CNR in images reconstructed using detectors with 2.5% and 3.0% energy resolution is 32% and 78% lower than the signal reconstructed with detectors with ideal energy response.

C. XFCT and Transmission CT Comparison

High-resolution phantom XFCT and transmission CT images and K-edge images are shown in Fig. 9. The images were generated using a full 2-cm-wide detector ring with ideal energy response detectors and using imaging dose of 2 mGy. Similar

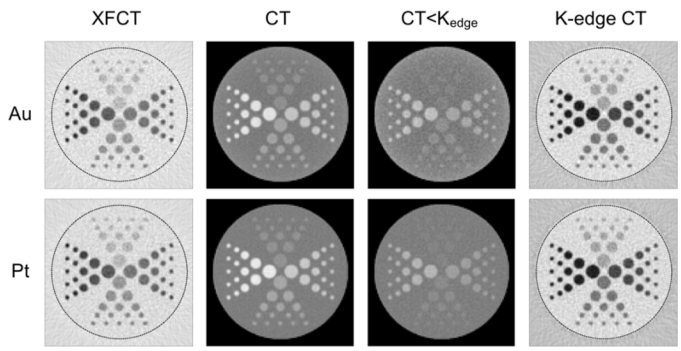

Fig. 9. Reconstructed images of the high-resolution phantom loaded with gold (top) and platinum (bottom). XFCT images (first column), transmission CT image generated using all X-rays (second column) and using X-rays below (third column) the respective K_{edge}. K-edge CT images (fourth column) are reconstructed by subtracting $C < K_{\mathrm{edge}}$ images form CT images. Transmission image W/L settings are 1000 and 0 and the full range of reconstructed values is displayed in contrast-only images.

to the low-resolution phantom, the contrast is higher in XFCT images of the phantom loaded with platinum. The noise in platinum images is also higher (first column of Fig. 9).

Transmission CT images are presented in the second to fourth columns of Fig. 9. As expected, CT images reconstructed using all photons (second column) have a higher contrast than CT images reconstructed using photons with energies below the K_{edge} of the contrast (third column). K-edge CT images (fourth column) generated by subtracting $\mathrm{CT} < K_{\mathrm{edge}}$ images from CT images show contrast-only images with subtracted phantom material.

CNR of XFCT images and transmission K-edge CT images for all combinations of contrast concentrations of 0.5%, 1%, 1.5%, and 2.0% and contrast vials of 1.5, 2.0, 3.0, 4.0, and 5.0 mm in diameter is shown in Fig. 10. All imaged objects have a CNR higher than 4 and are thus detectable. CNR of the vials varies from 6 to 26 in XFCT images and from 6 to 33 in CT K-edge images.

In general, CNR of XFCT images is lower than CNR of K-edge CT images. The differences between CNR of XFCT and K-edge images increase as the contrast agent concentration increases and the size of the vial increases. Whereas the CNR of the 1.5 mm vial filled with 0.5% contrast is comparable for both imaging techniques and contrast agents, the XFCT CNR of the 5 mm vial filled with 2% contrast is only 66% of the K-edge CT CNR.

Similar to the results of the low-resolution phantom study, CNR of gold XFCT images is on average slightly lower than CNR of platinum. CNR of K-edge CT images is also lower for gold than for platinum. A linear relationship between CNR and contrast agent concentration is observed for all sizes of vials in both XFCT and K-edge CT images. In XFCT images, CNR is constant for the 0.5% contrast concentration. For higher concentrations, CNR first increases as a function of vial diameter but it reaches a maximum at a certain size of vial. The concentration, at which CNR reaches its maximum, decreases with increasing vial size. This effect can be attributed to self-attenuation of fluorescence X-rays in larger vials and it is more pronounced for higher contrast concentrations.

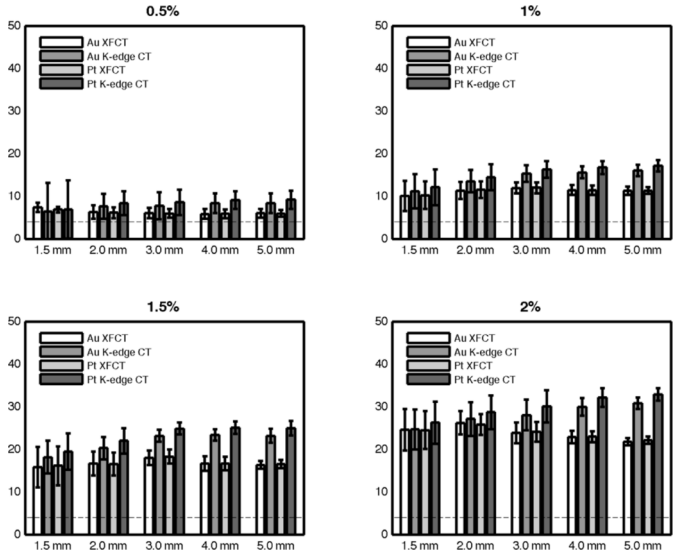

Fig. 10. CNR calculated from XFCT and K-edge CT images for various concentrations of gold and platinum as a function of contrast agent concentration and object size. Imaging dose is 2 mGy.

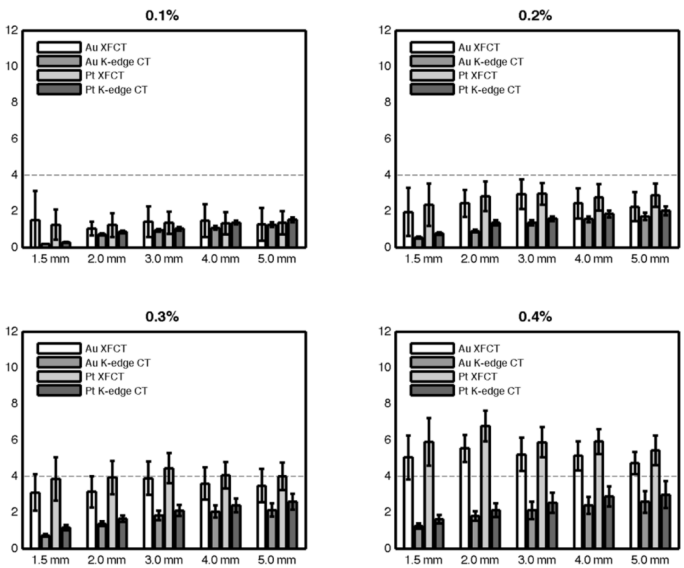

Fig. 11. CNR calculated from XFCT and K-edge CT images for various concentrations of gold and platinum as a function of contrast agent concentration and object size for concentration of 0.1%–0.4%. Imaging dose is 2 mGy.

CNR of XFCT images and transmission K-edge CT images for all combinations of contrast concentrations of 0.1%, 0.2%, 0.3%, and 0.4% and contrast vials of 1.5, 2.0, 3.0, 4.0, and 5.0 mm in diameter is shown in Fig. 11. All vials with 0.4% concentration and 2–4 mm Pt vials with 0.3% concentration are detectable in XFCT images and no vials are detectable in K-edge CT images. CNR of XFCT images is higher than CNR of K-edge CT images for all concentrations below 0.4%.

IV. Discussions

A Monte Carlo model of XFCT and transmission CT imaging was presented. First, the quality of XFCT images as a function of dose using a low-resolution phantom with 5 mm diameter objects loaded with contrast was studied. Based on Fig. 7 and Rose criterion, the minimum detectable concentration $c(\mathrm{CNR} = 4)$ can be expressed as a function of imaging dose D using $c(\%) = 0.608/D^{0.5}\ (\mathrm{mGy})$ and $c(\%) = 0.426/D^{0.5}\ (\mathrm{mGy})$ for gold and platinum, respectively. The lowest detectable concentration for a 5 mm sized object imaged with a dose of 10 cGy is 0.061% for gold and 0.042% for platinum. Typical clinically used Cisplatin concentrations are in the order of $10^{-4} - 10^{-3}\%$ [19], [20], which would not be detectable in our proposed setup.

The detector ring study shows how the CNR changes as a function of detector ring width, angular coverage, and energy resolution (Fig. 8). A linear relationship between the CNR and detector ring width and between the CNR and angular coverage are found. The CNR for various combinations of detector width and angular coverage can be calculated based on these relationships. The 1.1% energy resolution of the CdTe detector might not significantly affect imaging performance of the proposed XFCT imaging system using detectors with 1 keV energy bins. Note that the CNR would be larger for a setup with smaller energy bins. The spatial distribution of the detectors in the detector ring was not taken into account and no dead spaces were considered. This will further decrease the detected signal and image CNR. The magnitude of this effect can be estimated using plots in Fig. 8(b).

For the studied concentrations of 0.5%–2%, we show that K-edge imaging of gold nanoparticles and Cisplatin produces images with higher CNR than XFCT imaging. However, CNR differences between XFCT and K-edge CT images decrease with decreasing contrast concentrations and object size. For the 0.5% contrast and 1.5 mm object size, CNR of the two imaging techniques are practically equal. Our simulations show that for lower concentrations, CNR of XFCT images is higher than CNR of K-edge CT images. This can be attributed to the combination of higher noise in K-edge CT images compared to XFCT images and the imperfect subtraction of the background material. Unlike conventional transmission CT imaging, XFCT and K-edge imaging result in contrast-only images. CNR of XFCT does not depend on the background tissue type. On the other hand, the background tissue subtraction is not perfect in K-edge CT images, which causes a decrease in CNR for low concentrations compared to XFCT images.

An advantage of XFCT and K-edge CT imaging over conventional transmission CT imaging is imaging of contrast in the vicinity of bony tissue. We demonstrated this by simulating a bone phantom, in which 1-cm-diameter cortical bone insert was surrounded by a 3-mm-thick layer of 5.5% gold solution and another 1-cm-diameter mandible insert was surrounded by a layer of 4.5% gold solution [Fig. 12(a)]. The contrast agent concentrations and bone tissues were chosen such as their CT numbers in the conventional CT image are similar and it is not possible to separate the contrast agent from the bone tissue [Fig. 12(b)]. In XFCT and K-edge CT images, however, the spatial distribution and concentrations of the contrast agents can be clearly resolved [Fig. 12(c) and (d)]. With agreement to the previous studies, the high-concentration contrast agent has a better contrast on K-edge CT images than in XFCT images.

The results of conventional CT images and $\mathrm{CT} < K_{\mathrm{edge}}$ images are not shown. CNR of conventional CT images is

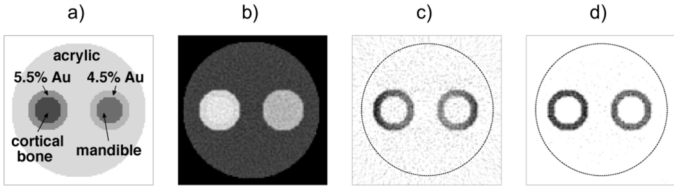

Fig. 12. The schematic of the bone phantom (a), its CT (b), XFCT (c), and K-edge CT (d) images.

lower for all vial sizes for 0.5% and 1.0% concentrations and for 1.5–3.0 mm vial sizes for 1.5% and 2% concentrations. For larger objects, the CNR is higher for conventional CT images. For the 0.5% concentration, vials with 1.5–3.0 mm diameters are not detectable in conventional CT images. CNR of $\mathrm{CT} < K_{\mathrm{edge}}$ images is lower than the CNR of XFCT images for all sizes and concentrations and object with concentrations below 1% are not detectable. As a result, CT imaging of gold nanoparticles and Cisplatin should not be performed with energies below the K_{edge} of gold and platinum.

It should be noted that the larger sized object are located in the center of the high-resolution phantom. Fluorescent X-rays will get attenuated in the phantom before they reach the detector ring, which causes a decrease in the reconstructed signal and subsequently the CNR of these objects decreases (Fig. 10). This effect is also visible in XFCT images of the low-resolution phantom in Fig. 6 where the signal on the periphery of each vial is higher than the signal towards the center of the phantom. The nonuniformity of the signal can be remedied by applying more sophisticated image reconstruction techniques, in which fluorescence X-ray attenuation in the phantom can be taken into account.

In previous works [3], [4], maximum likelihood (ML) algorithm [21] was used for image reconstruction of XFCT images due to the low count statistics. All images were reconstructed with a simple filtered back-projection (FBP) in this study. FBP was used to objectively compare XFCT images to transmission CT images.

We show that for the studied concentrations on the order of 0.5%–2.0%, K-edge CT images show a higher CNR than XFCT images. XFCT imaging is performed with energy-resolving detectors and the relative energy resolution should ideally be below 1% [Fig. 8(c)]. Multiplex imaging of multiple contrast agents can be then easily performed with XFCT. On the other hand, K-edge imaging can be performed with detectors equipped with only a single energy separator [22] making the imaging system less expensive.

XFCT data for image reconstruction (the energy spectra for each pencil beam position) contain X-ray fluorescence photons at the corresponding $K\alpha$ energies of the imaged element as well as Compton scatter photons. Compton scatter photons contaminate the signal and they have to be subtracted from the total number of $K\alpha$ counts. In our simulations assuming perfect energy response and 1 keV energy resolution, a simple linear interpolation using two neighboring energy bins was used. In a realistic scenario, more sophisticated interpolation techniques such as cubic spline using a number of neighboring energy bins will be used. Another approach to remove Compton scatter photons is the use of physical collimators or grids in front of the detector. This challenging technique results in lower detection efficiency and will be considered in our future work, in which fan beam and cone beam scanning will be investigated.

In practice, gold nanoparticles and Cisplatin will not only be taken up by tumors, they will also be present in normal tissue [23]. The effect of background concentration was not studied in this work, however, we would like to note that background concentrations will decrease the CNR of both XFCT and transmission CT images. Another consideration not taken into account in this work is the fact that the simulated phantom is uniform along the y-axis, the axis of rotation of the X-ray tube. To mimic real scenarios, a phantom heterogeneous in the direction along the axis of rotation should be simulated.

The quality of both XFCT and K-edge CT images is a function of the energy spectra used for imaging. As the energy decreases towards the K-edge, the image contrast increases. Image contrast also increases with a more monochromatic beam. Ideally, monochromatic source such as synchrotron radiation should be used for XFCT imaging to increase its sensitivity [24]. With our MC model, a compromise between image quality and imaging dose for XFCT imaging with an X-ray tube can be found. By up scaling the detector ring in the model, XFCT and K-edge CT imaging of patients can be simulated and studied.

V. Conclusion

A Monte Carlo model of an *in vivo* imaging system for X-ray fluorescence and K-edge CT imaging using a conventional X-ray tube and selective excitation has been presented. Based on our simulations, we have shown that XFCT outperforms K-edge CT for imaging of probes at low $(<0.4\%)$ concentrations. Unlike in conventional CT images, probe contrast in XFCT images is completely independent of the type of surrounding tissue. With the proposed system, anatomical CT and molecular XFCT images can be acquired simultaneously by separating transmission X-ray signal and probe fluorescent X-ray signal in the detector ring data. Further increase in sensitivity is expected when monoenergetic X-rays are used for excitations. This will be the subject of our future research.

Acknowledgment

The authors would like to thank Dr. B. Fahimian for his valuable discussions on the design of the proposed XFCT system.

References

[1] W. Cong, H. Shen, and G. Wang, "Spectrally resolving and scattering-compensated X-ray luminescence/fluorescence computed tomography," *J. Biomed. Opt.*, vol. 16, no. 6, pp. 066014-1–066014-7, Jun. 2011.

[2] G. Pratx *et al.*, "Tomographic molecular imaging of X-ray-excitable nanoparticles," *Opt. Lett.*, vol. 35, no. 20, pp. 3345–3347, Oct. 2010.

[3] G. Pratx *et al.*, "X-ray luminescence computed tomography via selective excitation: A feasibility study," *IEEE Trans. Med. Imag.*, vol. 29, no. 12, pp. 1992–1999, Dec. 2010.

[4] B. L. Jones and S. H. Cho, "The feasibility of polychromatic cone-beam X-ray fluorescence computed tomography (XFCT) imaging of gold nanoparticle-loaded objects: A Monte Carlo study," *Phys. Med. Biol.*, vol. 56, no. 12, pp. 3719–3730, Jun. 2011.

[5] S.-K. Cheong *et al.*, "X-ray fluorescence computed tomography (XFCT) imaging of gold nanoparticle-loaded objects using 110 kVp X-rays," *Phys. Med. Biol.*, vol. 55, no. 3, pp. 647–662, Feb. 2010.

[6] T. Takeda *et al.*, "X-ray fluorescent CT imaging of cerebral uptake of stable-iodine perfusion agent iodoamphetamine analog IMP in mice," *J. Synchrotron Radiat.*, vol. 16, pp. 57–62, Jan. 2009.

[7] R. Cesareo and S. Mascarenhas, "A new tomographic device based on the detection of fluorescent X-rays," *Nucl. Instrum. Methods Phys. Res.*, vol. 277, no. 2–3, pp. 669–672, May 1989.

[8] X. Huang *et al.*, "Gold nanoparticles: Interesting optical properties and recent applications in cancer diagnostic and therapy," *Nanomedicine*, vol. 2, no. 5, pp. 681–693, Oct. 2007.

[9] T. Boulikas and M. Vougiouka, "Cisplatin and platinum drugs at the molecular level (review)," *Oncol. Rep.*, vol. 10, no. 6, pp. 1663–1682, Nov.–Dec. 2003.

[10] T. R. C. Johnson *et al.*, "Material differentiation by dual energy CT: Initial experience," *Eur. Radiol.*, vol. 17, no. 6, pp. 1510–1517, Jun. 2007.

[11] A. N. Primak *et al.*, "Improved dual-energy material discrimination for dual-source CT by means of additional spectral filtration," *Med. Phys.*, vol. 36, no. 4, pp. 1359–1369, Apr. 2009.

[12] J. P. Schlomka *et al.*, "Experimental feasibility of multi-energy photon-counting K-edge imaging in pre-clinical computed tomography," *Phys. Med. Biol.*, vol. 53, no. 15, pp. 4031–4047, Aug. 2008.

[13] I. Kawrakow and D. W. O. Rogers, The EGSnrc code system: Monte Carlo simulation of electron and photon transport NRCC, 2006, PIRS-701.

[14] D. W. O. Rogers, B. Walters, and I. Kawrakow*, BEAMnrc Users Manual*. Ottawa, Canada: NRCC, 2006.

[15] B. R. B. Walters, I. Kawrakow, and D. W. O. Rogers*, DOSXYZnrc Users Manual*. Ottawa, Canada: NRCC, 2007.

[16] M. Bazalova and F. Verhaegen, "Monte Carlo simulation of a computed tomography X-ray tube," *Phys. Med. Biol.*, vol. 52, no. 19, pp. 5945–5955, Oct. 2007.

[17] A. C. Thompson *et al.*, "Computed-tomography using synchrotron radiation," *Nucl. Instrum. Methods Phys. Res.*, vol. 222, no. 1–2, pp. 319–323, 1984.

[18] A. Rose*, Vision: Human and Electronic*. New York: Plenum, 1973.

[19] J. Areberg *et al.*, "Gamma camera imaging of platinum in tumours and tissues of patients after administration of Pt-191-cisplatin," *Acta Oncologica*, vol. 38, no. 2, pp. 221–228, 1999.

[20] R. Jonson *et al.*, "Uptake and retention of platinum in patients undergoing Cisplatin therapy," *Acta Oncologica*, vol. 30, no. 3, pp. 315–319, 1991.

[21] L. A. Shepp and Y. Vardi, "Maximum likelihood reconstruction for emission tomography," *IEEE Trans. Med. Imag.*, vol. 1, no. 2, pp. 113–122, Oct. 1982.

[22] H. Tajima *et al.*, "Performance of a low noise front-end ASIC for Si/CdTe detectors in compton gamma-ray telescope," *IEEE Trans. Nucl. Sci.*, vol. 51, no. 3, pp. 842–847, Jun. 2004.

[23] J. F. Hainfeld, D. N. Slatkin, and H. M. Smilowitz, "The use of gold nanoparticles to enhance radiotherapy in mice," *Phys. Med. Biol.*, vol. 49, no. 18, pp. N309–N315, 2004.

[24] G. F. Rust and J. Weigelt, "X-ray fluorescent computer tomography with synchrotron radiation," *IEEE Trans. Nucl. Sci.*, vol. 45, no. 1, pp. 75–88, Feb. 1998.